FRICTION MEASUREMENTS USING MICROPIPETTES

FRICTION PROPERTIES OF POLYMER SYSTEMS AS MEASURED USING MICROPIPETTES

By

MARK ANTHONY HEALEY, B.Sc.

A Thesis
Submitted to the School of Graduate Studies
in Partial Fulfillment of the Requirements
for the Degree
Master of Science

McMaster University
©Copyright by Mark Anthony Healey, 2010.

MASTER OF SCIENCE (2010) McMaster University
(Physics) Hamilton, Ontario

TITLE: Friction Properties of Polymer Systems as Measured Using Micropipettes

AUTHOR: Mark Anthony Healey, B.Sc.(Memorial University of Newfoundland)

SUPERVISOR: Dr. Kari Dalnoki-Veress

NUMBER OF PAGES: ix, 51

Abstract

In this work, we tested the ability of an experimental system, involving the use of micropipettes as force transducers, to measure the coefficients of friction of several systems. Using a magnetic pipette puller, the micropipettes were produced by first heating and stretching the glass. The pipettes are then manipulated into an L-shape. This geometry allows one arm to act as the normal force transducer, and the other to act as the lateral force transducer for the purposes of friction measurements. We then analyzed the variation of the friction force of 15 μm polystyrene beads in contact with silicon and polystyrene in a fluid environment at increasing velocities. We also measured the variation in friction coefficient of poly(dimethyl siloxane) coated polystyrene beads in contact with a silicon surface. Our results were then compared to known values where possible, and the variation of the friction coefficient with increasing velocity was fit to a known phenomenological model. From our experiments, we have shown that our experimental technique can provide reproducible friction coefficient measurements, and these coefficients vary with velocity in a known manner. These results confirm the ability of micropipettes to act as both normal and lateral force transducers in friction experiments, and that they have the potential to be used in measuring friction coefficients of more complex materials.

Acknowledgements

The people I would like to thank are numerous so I'll just keep it simple. First, I'd like to thank Kari for giving me the opportunity to study under him at McMaster, as well as being patient and still knowing when I needed a swift kick to get back on track. His knowledge and passion for research are infectious, and make even the most difficult task more enjoyable. I would also like to thank Sara, Josh, Rob, Jessica, and Jerod for the atmosphere and kindness they provided through my time at McMaster.

I would also like to thank my fiancee Sharon for being such a supportive and understanding partner. Listening to me gripe when things weren't going right, helping me celebrate when things were successfull. Her understanding and thoughtfulness were instrumental in my completion of this work.

Finally, I would like to thank my family. For listening to me droan on about school even if they didn't know what I was talking about, but believing in me all the same. My Mom for her strong voice, and loving heart. My Dad for his quiet strength, and showing me how awesome reading and learning can be from a very young age. And both for their dedication to our family. My brothers, Christopher and Robert, for being there to pick on me or be picked on when I needed it of course.

Thank you all very much.

Contents

List of Figures

List of Tables

LIST OF TABLES

Chapter 1

Introduction

This work represents the culmination of experiments and research on the use of micropipettes as force transducers. The purpose of these experiments is to further understand, verify and improve on the method developed by Goulet and Dalnoki-Veress to measure the friction coefficients of living cells[1]. The micropipettes are borosilicate capillary tubes that have been elongated and bent into an L-shape, which allows them to produce both normal and lateral forces. The production and description of the fabricated micropipettes are given in Chapter 3. Instead of manipulating small single cells as in Goulet's research, we focused on working with small polystyrene (PS) and poly(dimethyl siloxane) (PDMS) coated PS beads in contact with a substrate as a basic, well understood friction system. This will lay ground work for the further study of the rich, dynamic components of cellular membranes in friction experiments.

For macroscopic objects, the force of friction experienced as two objects move laterally over one another depends only on the materials that are in contact and the

applied normal force. This is most generally described through Amoton's Law,

$$F_{friction} = \mu F_{Normal}, \tag{1.1}$$

where F_{Normal} is the applied force normal to the surface, $F_{friction}$ is the force of friction experienced by the two objects, and μ is the coefficient of friction which relates the two quantities. However, due to the complexity of living cells it is likely that the force of friction varies in a much more complicated fashion. Each cell consists of a variety of internal and external structures. By varying the external stimuli (chemical and physical environment) and measuring the friction coefficient of the cell, we can learn more about the dynamics governing cellular components. The use of PS beads in the experiments presented in this thesis allows us to work on the same scale as large living cells, but using materials with known properties of friction.

Typically, when speaking about friction, we refer to the static friction (F_s) and the kinetic (or sliding) friction (F_k). The static friction can be thought of as the force needed to move an object at rest relative to another object it is in contact with. The kinetic friction however refers to the force required to keep the object in motion. The static friction coefficient (μ_s) and the kinetic friction coefficient (μ_k) relate the normal force on the object to this lateral friction force. A typical Force vs. Time curve is shown in Figure 1.1. As the applied force on a resting object increases, it reaches a point where it overcomes F_s and slips and decreases towards the steady state situation in which sliding occurs and F_k takes over. The force of friction does

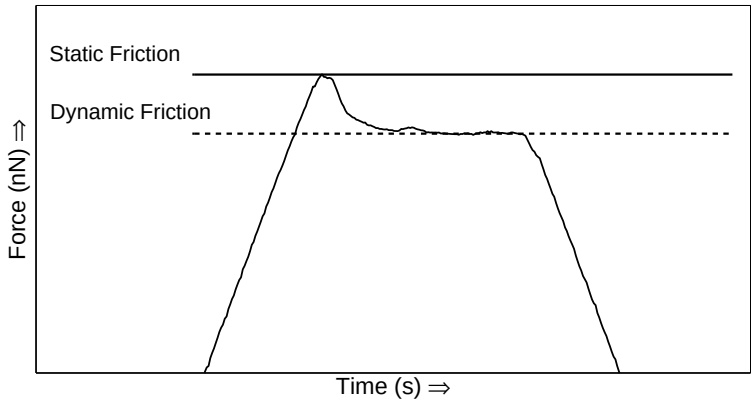

Figure 1.1: Force vs. Time curve showing the transition from the static friction regime to the kinetic friction.

not always decay from the maximum of the static friction to the dynamic friction regime. In some situations, phases of periodic stick followed by slipping may occur. In the stick phase, the relative motion of the two materials is zero. At the point of slip, the value of the applied lateral force becomes greater than the force of friction and the two objects move relative to one another. When an object is in the periodic stick-slip regime, the graph of the lateral force on the object appears as a sawtooth waveform, as shown in Figure 1.2. The periodicity of these events depends on both the applied normal force as well as the velocity. This process can extend its way down to the microscopic regime in which this work is based.

The work presented in this thesis has been built upon the previous work of Dr. Dalnoki-Veress' graduate students, Dr. Marie-Josee Colbert and Mr. Marc-Anton-Goulet. Colbert's worked delved into the development and study of a method to measure the strength of adhesion of single cells interacting with a substrate[2]. In her

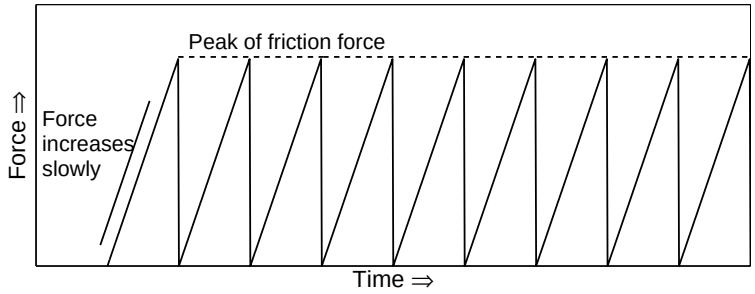

Figure 1.2: Force vs. Time curve showing the periodicity and force measurements during periodic stick-slip.

work, Colbert used an elongated pipette to measure this adhesion. The pipette used in Colbert's work was L-shaped, and consisted of a long arm (14 mm), and a short arm (0.5 mm). The longer arm was thin and flexible and provided the normal force. The shorter arm allowed the user to hold a bead into contact with a surface and to allow the force supplied by the longer arm to be directed normal to the substrate. Due to the shorter arm's length, it is much stiffer and does not interfere with the measurements of the force of adhesion.

Goulet presented the first attempt at measuring the response of living cells to the application of a friction force [1]. The data collected by Goulet showed variations in cellular response to friction under different conditions. These results indicated the potential of micropipettes force transducers to perform friction experiments with living cells. However, Goulet found that it was difficult to attain reproducible results. The method used by Goulet, and the method presented in this work are identical. However our work has focussed mainly on testing the instrument. Equipment testing was undertaken to better understand the measurement apparatus, as well as validating it

as a method of testing friction forces and to look to improve on its performance.

Chapter 2

Tribology

Tribology is the study of both the friction and wear of two surfaces in contact with one another [3]. In this section we will present several methods used in the study of friction, and ways in which they are used in modern experimental settings. The apparatuses presented are capable of measuring on the nano, micro and macroscopic scales. Tribometers capable of measuring on the macroscale range include the inclined plane tribometer, as well as the pin-on-disk tribometer. Whereas tribometers capable of measuring on the nano/microscale range include the surface forces apparatus and the friction force microscope (FFM).

2.1 Incline Plane Tribometer

The incline plane tribometer is a simple device, with a long standing history of use. Its applicability on the macroscopic scale lies in both its simplicity and utility. A schematic of the tribometer is shown in Figure 2.1. The inclined plane

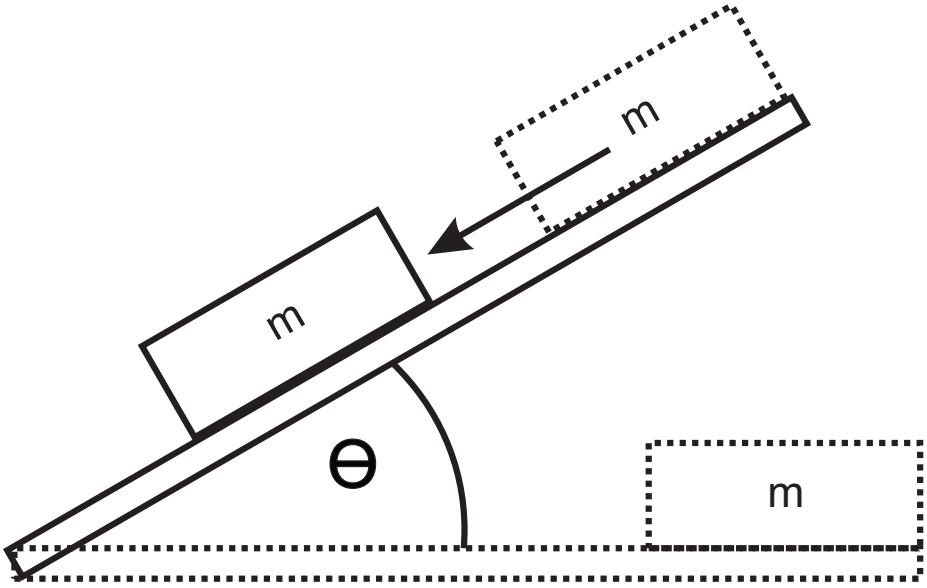

Figure 2.1: Incline tribometers operate by simply increasing the angle Θ until mass m begins to move.

tribometer consists of a plane that is capable of rotating about one axis. The rotation is accomplished by a motor or micrometer placed at one end of the plane that allows the user to vary the inclination. In order to test the coefficient of friction between two materials, a mass is first placed on the end of the plane where the motor/micrometer is attached. The inclination of the plane is then increased until the mass begins to move[3]. At this point, the force lateral to the surface exceeds the force of static friction,

$$F_{lateral} \geq \mu_s F_{Normal}, \tag{2.1}$$

where μ_s represents the coefficient of static friction, $F_{lateral}$ is the force of friction along the surface of the plane, and F_{Normal} is the force of gravity normal to the surface of

the plane. From the geometry of the plane, we determine μ_s to be,

$$\mu_s = \tan(\Theta). \tag{2.2}$$

Even as a simple device, the incline plane tribometer still has uses in modern research. For example, in a recent study by Burton *et al.* the authors used an inclined plane tribometer to examine the variation of the static friction coefficient of steal bearings in a cryogenic vacuum[4]. The authors lowered the initial temperature to 4 K and measured μ_s at various increasing temperatures.

2.2 Pin-on-Disk Tribometer

The pin-on-disk tribometer is another example of a simple, but commonly used method to determine friction properties of various pairs of materials. A schematic of this tribometer is shown in Figure 2.2. The pin-on-disk tribometer consists of an elastic arm attached to a strain gauge at one end and extending above a small disk. Through the end of the arm, a small inelastic pin is placed at a point above the disk. The normal force is determined by the application of a small mass above this pin. The tip of the pin is then placed in contact with the disk, which is placed on a rotating shaft. As the shaft rotates, the friction experienced between the pin and the disk is measured through the elastic deformation of the arm attached to a strain gauge[3]. The pin-on-disk tribometer can operate in two modes, bi-directional (oscillating) and

unidirectional. The user is also capable of measuring the amount of wear by analyzing the amount of material transferred from the pin to the disk. These tribometers have been used in many modern experiments, including biological [5] and soft matter [6].

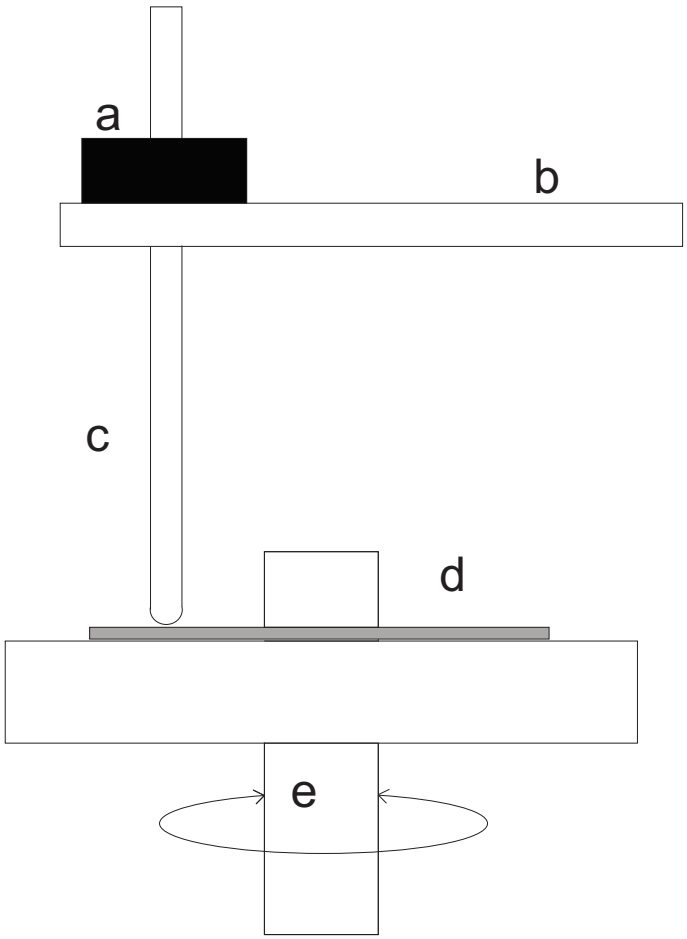

Figure 2.2: This schematic shows all of the major components of the pin-on-disk tribometer including ⓐ the loaded mass to provide a measureable normal force, ⓑ the elastic arm, ⓒ the pin, ⓓ the disk, and ⓔ the rotating base. As adapted from Shi *et al.*[5].

2.3 Surface Forces Apparatus

The original surface forces apparatus (SFA) was developed by Tabor, Winterton, and Isrealchvilli in the 1970's. The SFA consists of two crossed cylinders brought into contact with one another (Figure 2.3). The upper cylinder is slowly brought into contact with the lower one, while the distance between the two cylinders is measured using a multiple beam interferometric method known as fringes of equal chromatic order (FECO). Once the two cylinders come into contact, the force of this contact

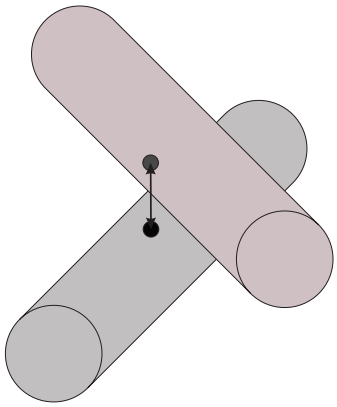

Figure 2.3: Schematic of contact cylinders.

is measured through the use of cantilever springs and strain gauges. Typically, the load is applied for a short time, where after (for a standard SFA) the cylinders are removed from one another and the force of adhesion/repulsion is again recorded by the strain gauges. In a friction experiment, a second motor (or micrometer) is added to allow the top cylinder to move in the lateral direction along the lower cylinder. Another set of strain gauges and springs is used to measure this lateral force and deflection. From this data, it is possible to attain high levels of precision in friction

testing for microscopic materials [7]. The surface force apparatus has been used to analyze the friction properties of a number of various systems, including surfactant monolayers[8], liquid crystals[9], and grafted polyelectrolytes[10].

2.4 Friction Force Microscopy

Friction force microscopy (FFM) is an extension of Atomic Force Microscopy. The FFM is capable of measuring small variations in friction over a surface at the atomic scale. The first successful measurements of atomic scale friction were performed by Mate *et al.* [11]. In their work, the experiments used a tungsten tip bent at 90° to the surface to measure the friction properties of the tip interacting with a sheet of graphite. The authors found that the friction force was highly dependent on the lattice spacing of the associate material (in this case, graphite). Much like the AFM, the FFM typically uses a silicon, or silicon nitride cantilever with a sharp silicon or silicon nitride tip attached to its end. The normal force is supplied to the surface by a piezo electric transducer. The normal deflection (and therefore the normal force) as well as the friction force is measured through the use of a laser reflected off the cantilever onto a four quadrant photodiode[12]. This photodiode registers a voltage that depends on the position of the reflected laser light onto its surface. Alternatively, this deflection can be registered through the use of a piezoresistive gauge.

Chapter 3

Experimental Setup

In this section, we will first describe the various stages of micropipette production and sample preparation. We will then describe the general experimental setup as well as the execution of our experiments.

3.1 Micropipette Fabrication

The fabricated micropipettes in this work act as both the lateral and normal force transducers in our experiments. The ability to produce these forces accomplished through the production of an L-shaped, elongated, narrow pipette which is schematically shown in Figure 3.1. We first begin with standard micropipettes with an inner diameter (ID) of 0.5 mm, and an outer diameter (OD) of 1.0 mm. In order to produce the thin ($\approx 10\mu$m) opening, we first stretch the pipette using a magnetic pipette puller (Narishige PN-30 Micropipette Puller). The puller is composed of a platinum heater plate, a sliding stage, and a magnetic solenoid. The platinum plate is formed

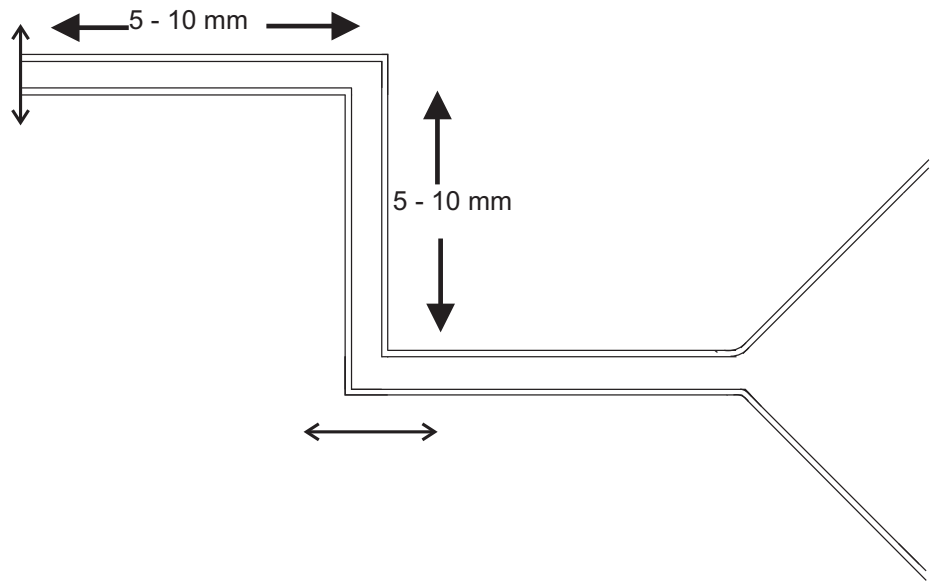

Figure 3.1: The L-shaped fabricated micropipette allows for deflection in the lateral and normal directions.

into a a semicircular geometry to supply uniform heating around the micropipette. The micropipette is held onto the sliding stage through the use of a small gripping screw, and then slid through the platinum heating element, and held into place at the other end by a similar screw on a non-moving stage. Current supplied to the puller heats the platinum plate, and also powers a magnetic solenoid. The solenoid produces an electromagnetic field used to provide a pulling force to the pipette as it is being heated. The heating of the pipette softens it, allowing it to be stretched and elongated by the force produced by the solenoid's magnetic field, which then breaks the pipette at a sharp tip. The pipette is then placed alongside a low powered microscope and manipulated by a translation stage set on a vertical shaft. This setup allows us to manipulate the pipettes position in the field of view of the microscope. A second

shaft is placed on the opposite side to hold a beam which secures a platinum/iridium wire (0.5 mm diameter) connected to the DC power supply (Xantrex HPD 30-10). We cleave the pipette to produce a clean cut section of glass by supplying a voltage across the wire which then heats the wire. The pipette tip is placed gently into contact with the heated wire. The power is then quickly shut off, and the glass is allowed to cool and contract which causes it to break. The L-shaped geometry of the pipette is produced by first replacing the 0.5 mm wire used in the cleaving stage with a 0.2 mm diameter platinum iridium wire. A low voltage (approximately 6 V) is then supplied to the wire. The cleaved pipette is brought approximately 1 cm across and into contact with the wire. Using a manipulator fashioned in lab, the micropipette is bent 90 ° at the point of contact with the heated wire. The pipette is then removed from the wire and moved so that a second bend can be made. This bend is made in the same fashion as the first, but in the opposite direction in order to produce the L-shape. Special attention is paid to keeping the two arms in the same plane.

3.2 Micropipette Calibration

Our micropipette geometry allows it to deflect in both the lateral and normal directions. We can determine the deflections of these two arms under small loads by

approximating it as a Hookean spring system,

$$F = k\Delta x; \tag{3.1}$$

where the spring coefficient k is experimentally determined as follows. We take our fabricated micropipette, and attach it to a 60 cc syringe by a thin rubber tube. The pipette is then positioned in front of a mirrored surface that has been placed on an inverted microscope (Olympus IX71 Inverted Microscope) stage and angled 45° to the surface of the stage. Water is then injected through the pipette using the syringe. This produces a roughly ellipsoidal drop about the micropipette tip. Several examples of this are given in Figures 3.2 and 3.3. We can then view the

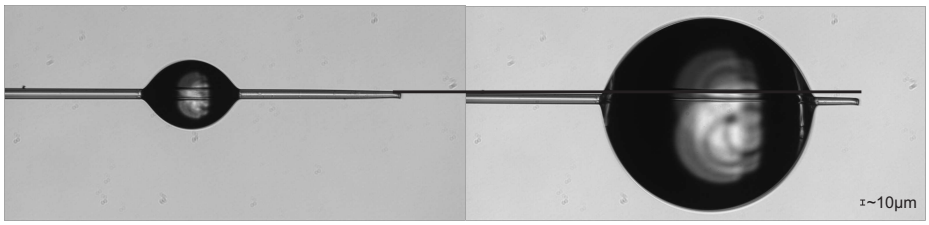

Figure 3.2: A micropipette with a spring constant of $0.033\pm0.005\mu$N/μm, deflecting due to a change in the water volume encompassing it.

reflection of the micropipette on the surface of the silicon mirror by positioning an external light source directed at the micropipette to the mirror, as shown in Figure 3.4. The reflection of the micropipette is recorded through the use of a digital camera (QImaging Mono 12 BII) attached to the base of the microscope. We then allow the water on the pipette to evaporate and monitor the deflection of the micropipette by

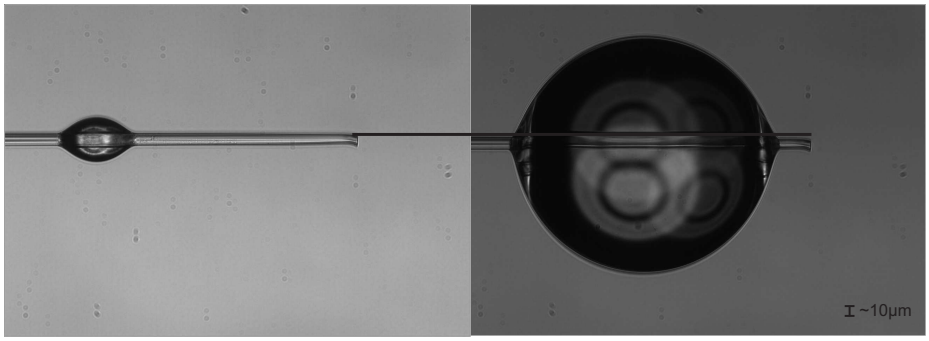

Figure 3.3: A micropipette with a spring constant of $0.09 \pm 0.01 \mu$N/μm, deflecting due to a change in the water volume encompassing it.

using 1D image correlation (to be discussed in the next section). The change in force due to this volume change can be expressed by,

$$\Delta F = (V_f - V_i)\rho_{water} g, \tag{3.2}$$

where ρ represents the density of water, g being the gravitational constant (9.81 m/s^2), and V_i being the initial volume and V_f the final volume of water. This method is then applied to obtain the spring constant of the arm producing the normal force by simply aligning the micropipette perpendicular to the surface of the microscope stage, and following the same procedure as for the lateral arm. An example of the data for the calibration is shown in Figure 3.5. The spring constants of our calibrated micropipettes ranged from 1×10^{-3} μN/μm to 1 μN/μm.

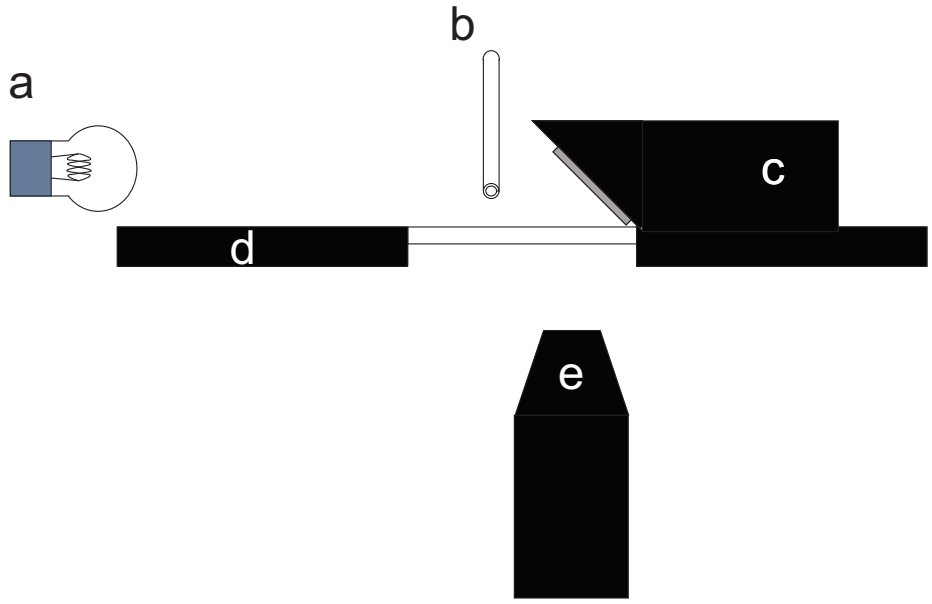

Figure 3.4: A schematic of the calibration setup for our micropipette. The external light source ⓐ provides the light for the microscope objective ⓔ, which allows us to view the reflected image of the micropipette ⓑ on the mirrored surface attached to a base ⓒ.

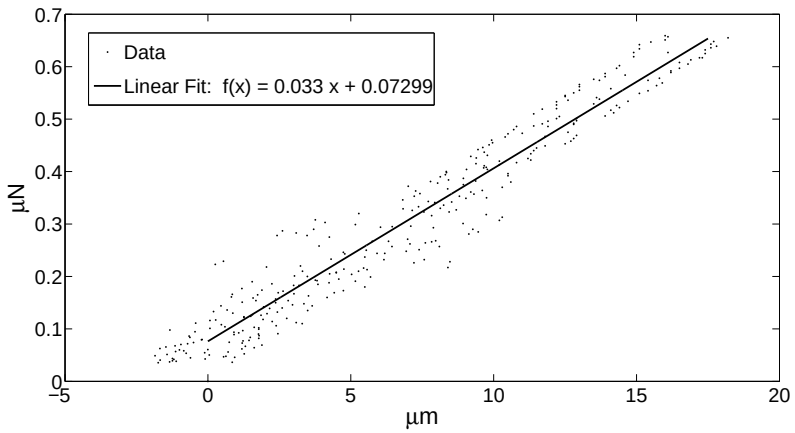

Figure 3.5: Data from the calibration of the lateral force producing arm of a fabricated micropipette.

3.3 Image Correlation

In order to measure the small displacements presented by our experimental setup, we analyzed the images collected by a digital camera using image correlation. Image

correlation is a common method used to analyze variations in change of position and strain of objects represented through an image series. These measurements are accomplished through the comparison of the pixel intensity of each image. The motivation for image correlation begins with considering the Euclidean distance,

$$d^2_{f,t}(u,v) = \sum_{x,y} \left[f(x,y) - t(x-u, y-v)\right]^2 \tag{3.3}$$

$$= \sum_{x,y} [f^2(x,y) + t^2(x-u, y-v) - 2f(x,y)t(x-y, y-v)] \tag{3.4}$$

where t is the pixel intensity array of the template region (the pattern we are trying to detect), and f is the pixel intensity array of the image we are searching. The sum is taken over the area of the template region at position (u, v)[13][14]. For constant values of $f^2(x,y)$ and $t^2(x-u, y-v)$, the remaining term,

$$c(u,v) = \sum_{x,y} f(x,y)t(x-u, y-v), \tag{3.5}$$

represents the *cross correlation coefficient* at position (u, v), and therefore the degree of similarity between the two images[13].

3.3.1 One Dimensional Image Correlation

For performing 1D image correlation, the initial image is first analyzed by indicating a line upon which the pixel intensity is to be analyzed. The intensity of each pixel

on this line is then recorded. This intensity is then compared to the pixel intensity values on the next image in the sequence on the same line, whereby the correlation coefficient at each pixel is determined by,

$$\Phi_{j,j+1}(t) = \sum_k f_j[k] f_{j+1}[k+t], \tag{3.6}$$

where $\Phi_{j,j+1}$ is the value of the correlation coefficient between images j, and $j+1$ at pixel t. The value of this function along the line gives us the distribution of correlation coefficients, which is equivalent to the square of the intensity. The pixel at which the peak of this spectrum occurs gives the position of highest correlation between images j and $j+1$. The position of this peak represents the position of the pipette in the next image [2]. To improve accuracy, a gaussian distribution is fit about this pixel, where the peak of the distribution represents the sub-pixel resolution. An example of the fit, as well as the correlation values and pixel intensity plots is shown in Figure 3.6.

3.3.2 Two Dimensional Cross Correlation

Two dimensional cross correlation is performed in a similar manner as the one dimensional case. The first step is to open the initial image in the sequence. From this image, a search space (or feature region) is defined by choosing a large rectangular area. This space will represent the position and area of each image to search. Next,

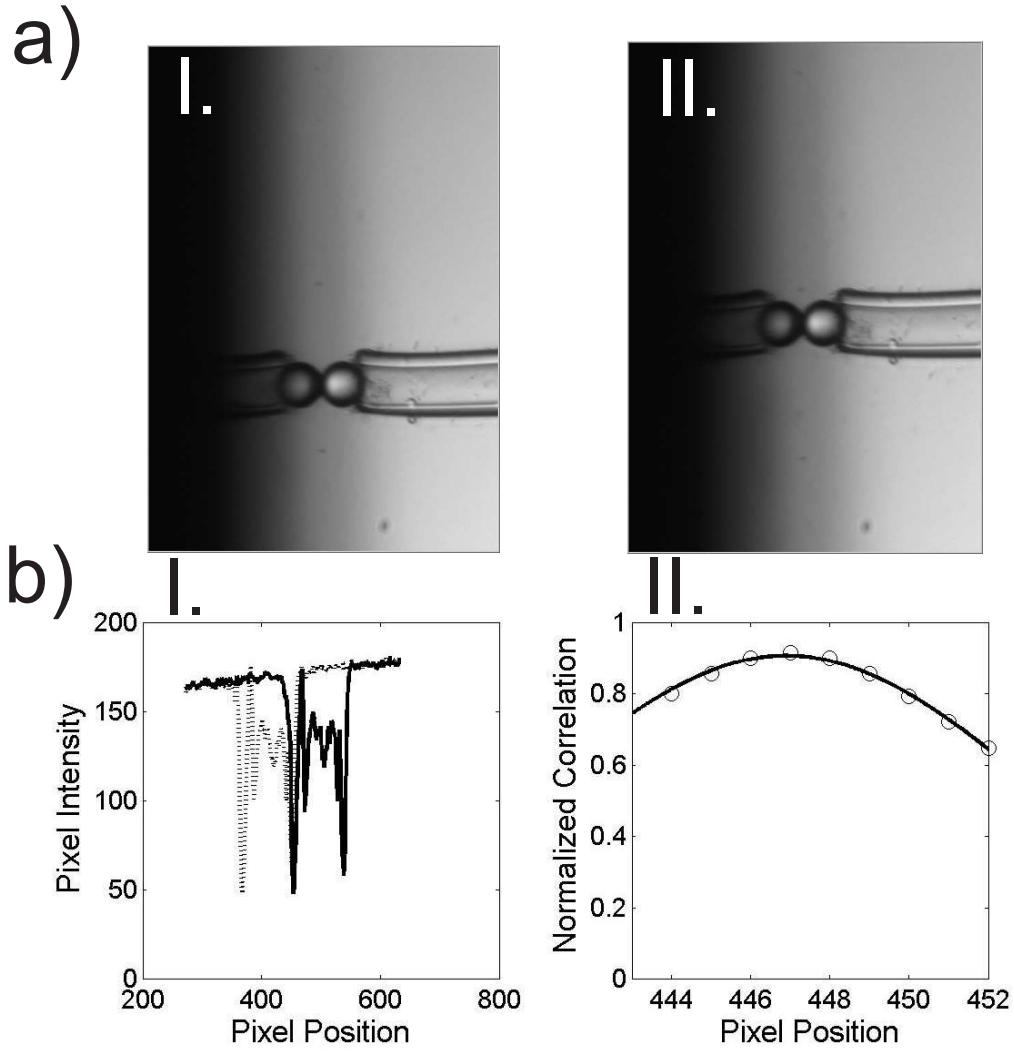

Figure 3.6: ⓐ Two images to be cross correlated (I and II). ⓑ Graph I represents the one dimensional pixel intensity plots for image the images in ⓐ. The normalized correlation values are then plotted in II. In this graph, we only show the distribution of correlation values for pixels about the max correlation. A gaussian distribution (solid line) is then fit to these correlation values, and the peak of this distribution represents the position of highest correlation, and therefore the pipettes new position.

a smaller template rectangle is chosen and represents the region that we are trying to track through the feature region. As the template is traced through the search space, the normalised cross correlation coefficient is calculated from,

$$\gamma(u,v) = \frac{\sum_{x,y}[f(x,y) - \overline{f}_{u,v}][t(x-u,y-v) - \overline{t}]}{(\sum_{x,y}[f(x,y) - \overline{f}_{u,v}]^2[t(x-u,y-v) - \overline{t}]^2)^{0.5}}, \tag{3.7}$$

where the sum, $f(x,y)$ and $t(x-u,y-v)$ are the same functions as described in Equation 4.5. The overbars on the functions represent the average pixel intensity for the region covered by the sum over x and y. This is normally accomplished through the equation,

$$\overline{f}_{u,v} = \frac{1}{N_x N_y} \sum_{x=u}^{u+N_x-1} \sum_{y=v}^{v+N_y-1} f(x,y), \tag{3.8}$$

which allows us to get a value for the normalized correlation coefficient between the search space of the image, and the template that we are trying to detect[13]. From the position with the highest level of correlation, we can then determine the position of our template in the new image. Initially, two dimensional cross correlation was used to determine the normal deflection of the bead and pipette as well as the lateral deflection. However, we found that two dimensional correlation was very consistent/accurate with the lateral deflection and less so for the normal deflection. This is most likely due to the fact that the normal deflection was varied a minute amount (0.05 to 0.25 μm), making it very difficult to differentiate the new position from the old. The lateral deflection on the other hand was typically much larger

and therefore changes were easier to detect. We then turned to using the motion of the motor to supply us with the deflection information relative to the position of first contact. This allowed much greater accuracy in the measurement of the relative normal deflection as the motor exhibits a movement accuracy of approximately 3×10^{-2} μm.

3.4 Sample Preparation

In this section, we will discuss how we prepared the samples used in our experiments. The discussion will include outlining how the substrates were produced, as well as the process of producing a polymer thin film on these substrates and coating our PS beads in PDMS.

3.4.1 Silicon Wafers

For our experiment, the substrate attached to the moving arm consisted of a 1 mm x 10 mm slice of Si(100). The slice was produced with the following procedure. Initially, the Si wafer was removed from the case and placed on lens paper, reflective side down. The lens paper itself is semi-transparent so it was moved to a sheet of gridlined (1 cm x 1 cm) paper. The straight cut on the wafer indicating the lattice orientation was aligned with a vertical line segment of the paper, and using a diamond scribe and a ruler, a line was scribed along the direction of the vertical line segments.

This process was then repeated for the entire wafer in both the horizontal and vertical directions. The wafer was the then cleaved along these etched lines, and each cleaved portion was transferred to a new sheet of lens paper to minimize interaction of the reflective layer with any formed silicon dust. These newly cleaved 1 cm^2 pieces of our silicon wafer were then transferred to a new sheet of lens paper and placed on a new grid consisting of 1 mm^2 squares. The silicon was then cleaved in only one direction to produce the 1 mm x 10 mm slivers that were required. They were then blown free of any dust remnants through the use of an argon jet.

3.4.2 Polystyrene Thin Films

Polystyrene (PS) is a long chain, non-polar polymer consisting of a carbon backbone and an aromatic side chain. To produce thin films of this material, we followed a standard dip coating procedure. Dip coating was used instead of spin coating because the asymmetry of the silicon slice would result in non-uniform thin films. In order to dip coat our silicon slices, we first dissolved a small quantity of the polymer in a good solvent, toluene. This solution is then diluted to a weight percentage of 0.01 %. A thin slice of prepared silicon is then dipped into the solvent/polymer solution and removed, leaving a droplet of the solution on the silicon. Due to toluene's high volatility, it evaporates quickly, allowing the polymer to precipitate out of solution and form a thin film on the surface of less than 100 nm. The approximate height of the film was determined by comparing interference patterns of our film with that of

prepared films of known height.

3.4.3 Poly(dimethyl siloxane) Coated Polystyrene Beads

Poly(dimethyl siloxane) (PDMS) is a long chain, hydrophobic polymer. For our purposes, we purchased a quantity of SYLGARD®184 from Dow Corning Ltd. SYLGARD®consists of a base mixture of PDMS, as well as a curing agent which allows the formation of crosslinks between the polymer chains so that it becomes a solid. The combination of PDMS and the curing agent allows us to produce a thin, solid coating on our PS beads that will change the beads surface properties. We first begin with a fabricated, calibrated micropipette set in the same vertical shaft as during the cleaving and manipulation. The micropipette is attached to a 60 cc syringe to supply suction. A small well containing a solution of the 15 μm diameter PS beads is placed within the field of view of a low powered microscope. The micropipette is then brought into the viewing area and lowered into the solution, where a PS bead is grasped and held onto with suction supplied by the syringe. The micropipette and the bead are then removed from the solution. The same wire/power setup used in the cleavage stage of fabrication is used to weld the PS bead to the tip of the micropipette. Welding was accomplished supplying a voltage to the wire and bringing the bead into close proximity with the wire and allowing it to slightly melt. This ensures the bead is stable and in a fixed position. The micropipette is then lowered into the SYLGARD®184 solution so that approximately 1 mm is immersed and re-

moved. It is then placed into an oven set at 90 °C for one hour to allow the PDMS to cure and harden.

3.5 Experimental Apparatus and Procedure

The main portion of our apparatus consists of an antivibration table, an inverted microscope, and shafts located to the right and left of the microscope which hold the translation stages necessary to move the pipette and the substrate. The shafts and microscope are held in place on top of the antivibration table by screwing them to a steel sheet attached to the table. Photo's of the apparatus and experimental setup are given in Figure's 3.7, 3.8, and 3.9.

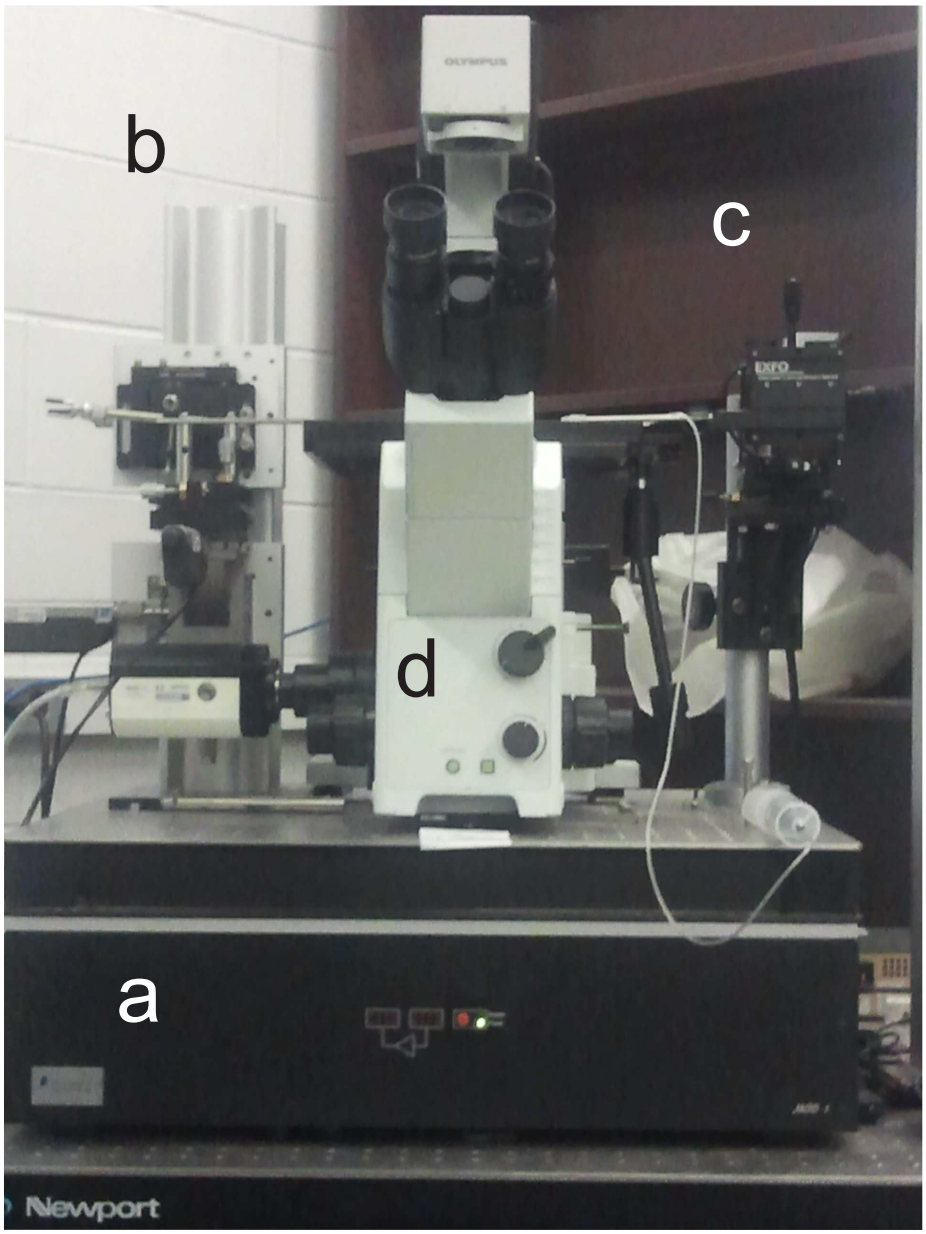

Figure 3.7: This figure shows a photo of the complete experimental setup. In this photo, ⓐ is the anti-vibration table, ⓑ is the vertical shaft supporting the motor and translational stage that move the substrate, ⓒ is the vertical shaft that holds the translational stage and micrometer that allow the manipulation of the fabricated pipette, and ⓓ is our inverted microscope.

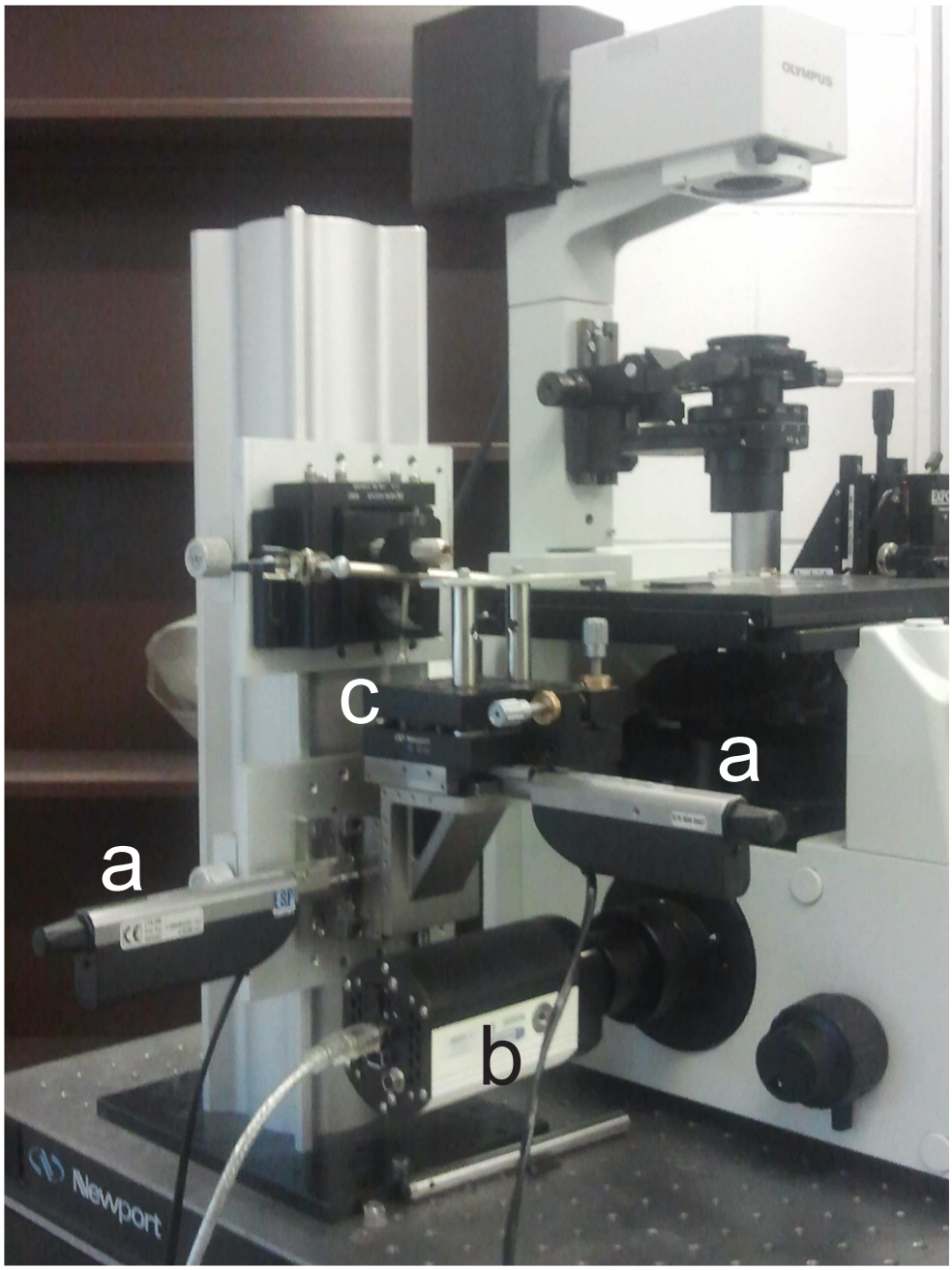

Figure 3.8: This figure shows the components of the vertical shaft that was to the left of the microscope in Figure 3.7. In this photo, ⓐ are the motors that allow the x-y motion of the substrate, ⓑ is the digital camera attached to the microscope, and ⓒ is the translation stage setup that allows variation in the pitch and yaw of the substrate.

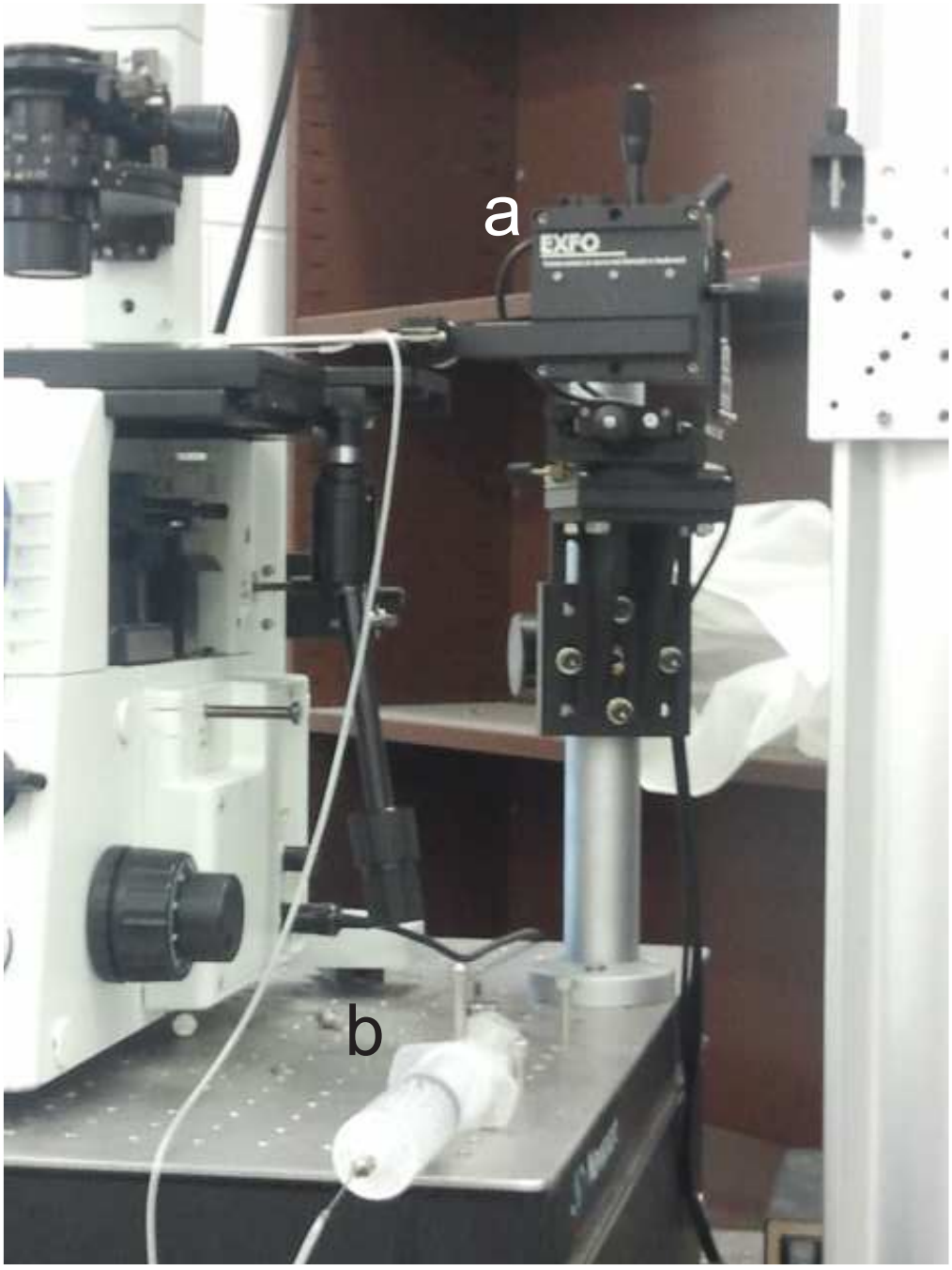

Figure 3.9: This figure shows the components of the vertical shaft that was to the right of the microscope in Figure 3.7. In this photo, ⓐ is the translation stage setup that allows the manipulation of our fabricated micropipette and ⓑ is the 60 cc syringe used to provide suction.

A fluid cell that will house the substrate and pipette is constructed of two slides spaced apart by small pieces of silicone, and held together by two small spring clamps. The fluid cell is then loaded on to a larger slide and held into place by double sided tape. The larger slide also has a magnet attached on the end opposite the fluid cell. The magnet is used to hold it into place on the microscope stage, where a second magnet is located. A dilute solution of 15 μm PS beads in Millipore water is loaded between the two slides and is held in place via capillary action. This fluid cell is then loaded onto the microscope stage. A schematic of the cell is given in Figure 3.10. The arm, which has the substrate attached on one end, is loaded on to the

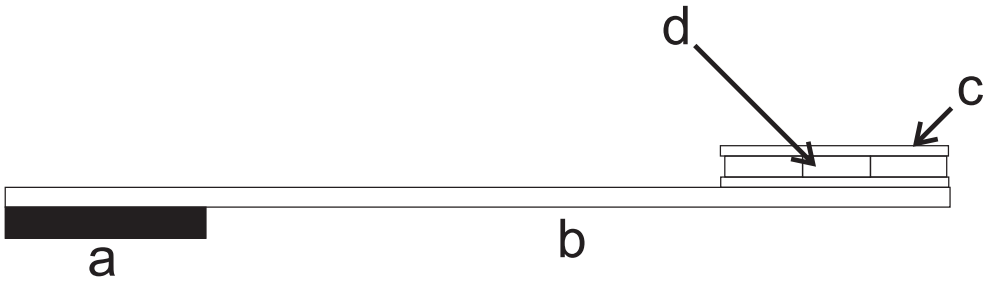

Figure 3.10: This figure shows the components of the fluid cell used to house the substrate and micropipette tip. ⓐ is the magnet attached the microscope slide ⓑ. The fluid cell is constructed from two microscope cover slips ⓒ, spaced apart by small pieces of silicone ⓓ.

translation stage setup on the right hand side of the microscope (Fig. 3.8). Using the motors, the substrate is then moved inside the fluid cell and into the viewing area of the microscope. The micropipette is then loaded with Millipore water by our 60cc syringe. This filled pipette is then placed onto a small beam and held secure by a screw clamp. The beam/pipette combination is then attached to the translation

stage on the right hand side of the microscope (Fig. 3.9), and held in place by a spring clamp. Then, using the same translation stage, the pipette was moved into the viewing area of the microscope, where a PS bead is grasped using suction from the syringe. The plunger of the syringe is then held into position to maintain suction. The pitch of the substrate is changed so that a reflection can be seen on the surface of our substrate (Figure 3.12) so that we can see when contact occurs. To make sure that the surface of the substrate is moving strictly perpendicular to the pipette, we first move the substrate in close enough to the PS bead so that an image can be seen. This image is then recorded, and the substrate is moved in the y-direction (Figure 3.11) by 0.5 to 1.0 mm. A second image is then recorded at the new position. Using the image analysis program ImageJ, we then measure the distance between the bead and its reflection for both of these images. If the distances are different, we alter the yaw of the substrate and repeat the process until the measurements are the same. If a slope is present, this would result in an asymmetric normal force and lateral force as the substrate was moved during each experiment, and this process allows us to minimize or eliminate this potential source of error.

In order to maximise the symmetry of the lateral deflections of our micropipettes, the substrate is brought into contact with the PS bead using a program written in Labview ("MAfrictionloops.vi") by a previous graduate student (Marc Antoni Goulet). The substrate is then moved in an oscillating fashion about this equilibrium point and the deflection is quickly measured via one dimensional image correlation. If the vari-

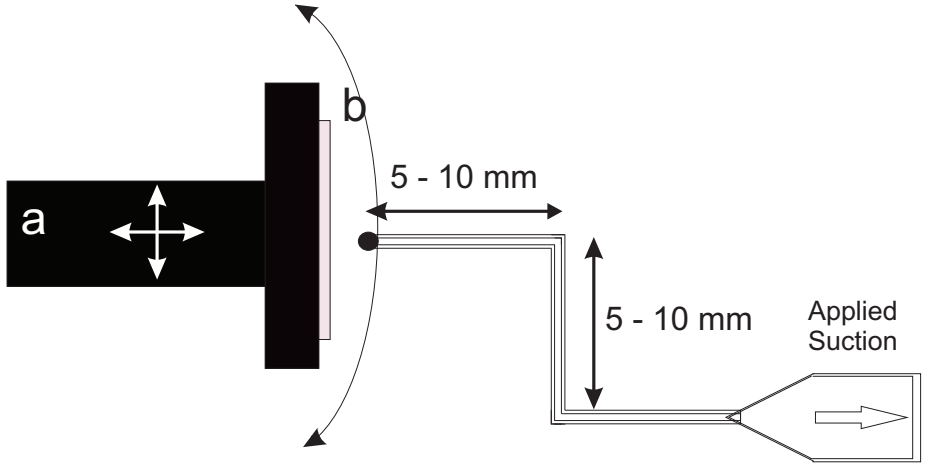

Figure 3.11: An overhead schematic of the fluid cell, showing the movement capabilities of the substrate arm, and the orientation of our micropipette.

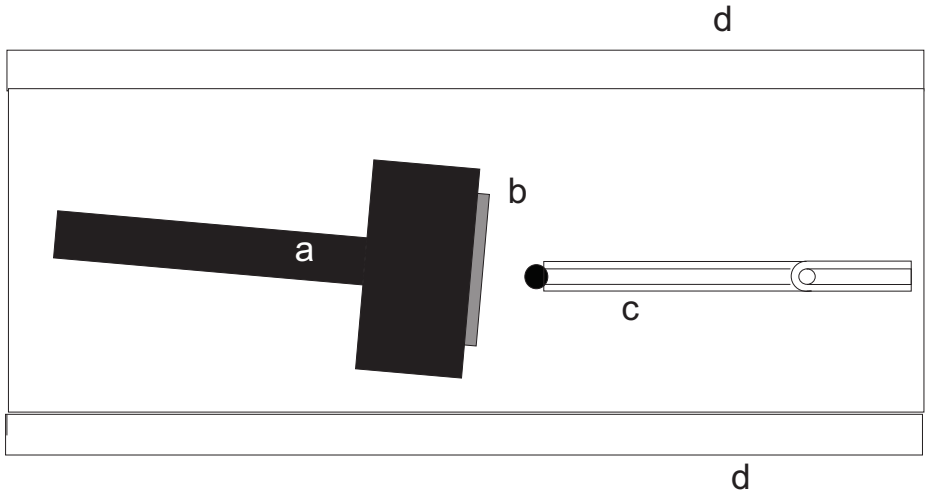

Figure 3.12: A sideview schematic of the fluid cell, showing the orientation of the substrate ⓑ attached to a movable arm ⓐ, with the micropipette ⓒ between two glass slides ⓓ.

ation is asymmetric, we then alter the angle of attack of the micropipette by manual manipulation of the right translation stage until a symmetric distribution is recorded. Examples of symmetric and asymmetric distributions are shown in Figure's 3.13 and

3.14 respectively. The asymmetry can be regarded as evidence that the normal force is not directed along the lateral arm, or that the spring constant of the pipette is asymmetric in the direction of deflection.

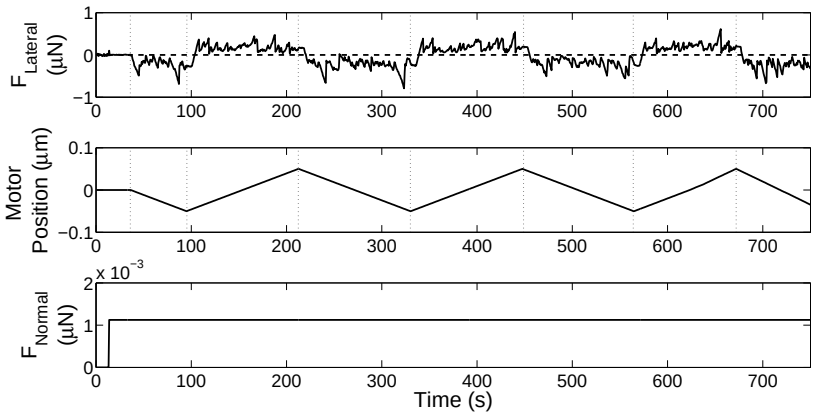

Figure 3.13: An example image of symmetric lateral force data (top) and normal force (bottom) from a PS on PS test run. The vertical dashed lines represent the change of direction of the substrates motion.

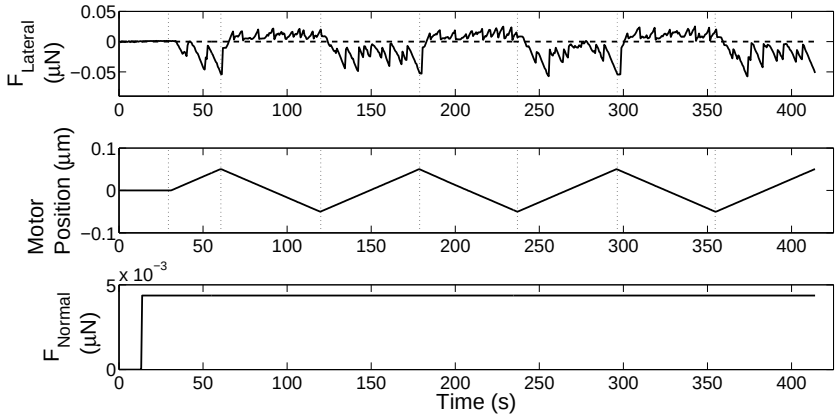

Figure 3.14: An example image of asymmetric lateral force data (top) and increasing normal force (bottom) from a PS on PS test run. The vertical dashed lines represent the change of direction of the substrates motion.

The experimental runs are performed in a similar fashion as the angle of attack tests. The substrate is first brought into contact with the bead attached to the micropipette tip, and this position is noted as our equilibrium point and our zero valued normal deflection. The substrate is then moved in an oscillating fashion about this position for a set number of loops, whereafter the substrate is moved towards the pipette to increase the normal deflection. This process is then repeated for the duration of each experimental run for 10 to 20 loops, with normal deflections varying by 0.05 μm to 0.25 μm every 1 to 4 loops. The PDMS coated PS bead experiments are run in basically the same fashion, except the bead is welded onto the micropipette prior to being placed inside the fluid cell.

Chapter 4

Results

In this chapter, we will describe the results of our friction tests on the interaction of several systems. The systems that we tested were,

1. Polystyrene bead in contact with a silicon surface.

2. Polystyrene bead in contact with a polysterene thin film.

3. PDMS coated PS bead in contact with a silicon surface.

In each of the systems studied, we attempted to maintain symmetric data to the best of our ability. For the analysis, we averaged the positive and negative lateral deflection for each normal deflection applied and found the half peak-to-peak lateral deflection (Δx_{HP2P}). Using Equation 3.1, we can obtain the lateral and normal forces under the average deflection. The lateral and normal forces are then fit to Equation 1.1 to determine the coefficient of friction for each experimental run. This was repeated several times, and the average value $\pm$ one standard deviation are shown in the results section for each system we studied.

4.1 Polystyrene Beads on a Silicon Surface

Initially, the testing of the experimental setup was performed with the simplest available system. This system consisted of a PS bead in contact with a silicon wafer in a simple fluid (Millipore water) environment. The method employed was capable of extracting symmetric results. It was found that small amounts of asymmetry in our lateral deflection data was still capable of producing consistent results, however the larger the asymmetry, the more erratic the measured results became. Data was collected using the previously outline method at 1, 2, 4, 6, and 8 μm/s. An example of the collected raw data for a single run is shown in Figure 4.1, noting the mostly symmetric distribution of the data.

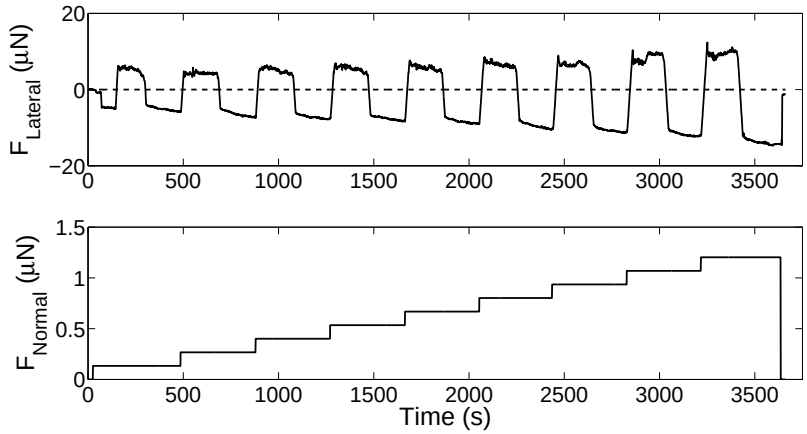

Figure 4.1: An example image of the collected raw data. The top graph represents the force caused by the lateral deflection of the pipette, and the bottom graph represents the increasing normal force.

The average collected values of the static coefficient of frictions for the 1 μm/s runs were found to be 0.176±0.006, where the dry values are 0.30±0.02[15]. The

difference between our experimentally determined coefficient of friction compared to the known dry friction value shows that a lubricating water layer was present in our experiments. As the velocity increases, the value of the friction coefficient was shown to decrease, which is qualitatively similiar with previous measurements by Maeda et. al [16]. In that work, the authors analyzed friction properties of polymers on polymer systems using a SFA. A plot of the velocity dependence of our measured coefficient of friction is shown in Figure 4.2. We can see from Figure 4.2 that the coefficient of

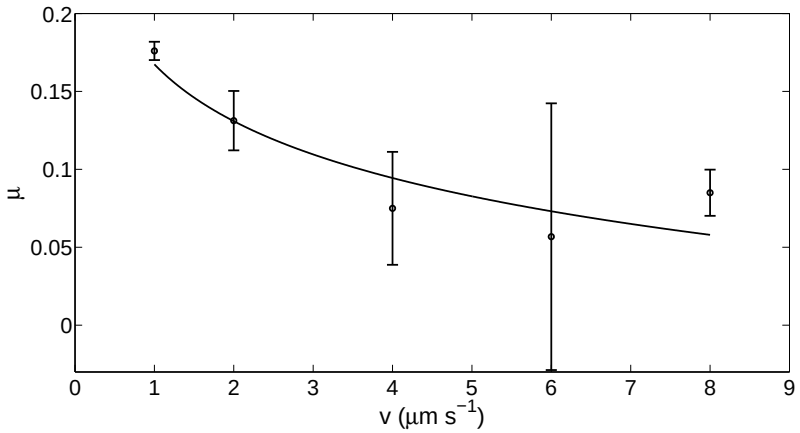

Figure 4.2: Decay of the coefficient of static friction with increasing velocity for PS on Si. Solid line added as a visual guide.

friction decays to a value of 0.085±0.02 at 8 μm/s, or by a factor of 2, as the velocity was increased from 1 μm/s.

4.2 Polystyrene Beads on a Polystyrene Surface

As with the PS on Si system, the PS on PS system showed a decreasing friction coefficient with increasing velocity. At 1 μm/s the value of the friction coefficient was shown to be 0.49±0.11, with the dry friction value being 0.50±0.02[17]. The reason for our ability to reproduce the dry friction value in an aqueous environment is most likely due to the hydrophobicity of both the bead and the substrate. This hydrophobic quality of the materials allows the water layer to be forced from between the two surfaces with much less force then the PS on Si system. The PS on PS system also exhibited a faster decrease of the friction coefficient then the PS on Si system as the velocity increased. In Figure 4.3 we show the data for coefficient of static friction vs. velocity.

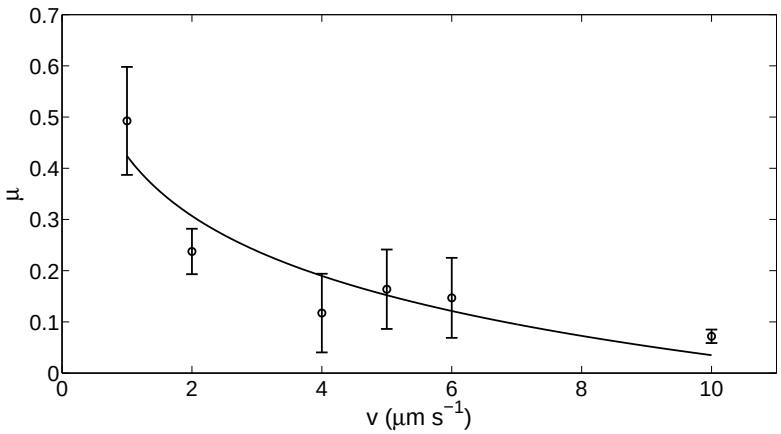

Figure 4.3: Decay of the coefficient of static friction with increasing velocity for PS on PS. Solid line added as a visual guide.

This figure is consistent with that of PS on Si, where we see that the friction

coefficient decreases with increasing velocity. The coefficient in this case decreases from 0.49±0.11 to 0.07±0.01, or by a factor of 7.

4.3 Poly(dimethyl siloxane) Coated Polystyrene Beads on a Silicon Surface

For our third system, we first note that the value of the coefficient of friction for the PDMS is generally very low, making it a useful coating for many surfaces. The coefficient of friction noted in the literature for a PDMS elastomer on Silicon in deionized water has been shown to be slightly less then 0.1[18], where our measurements at 1 μm/s resulted in $\mu_s = 0.07 \pm 0.05$. As the velocity is increased to 10 μm/s, the value of the friction coefficient decreases to 0.02±0.01.

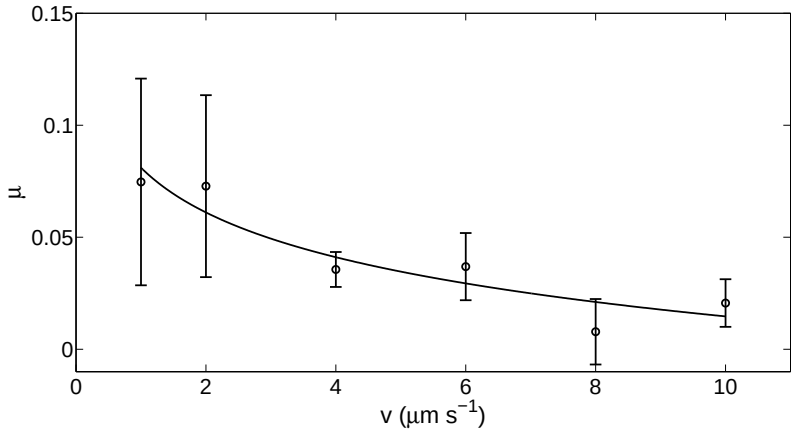

Figure 4.4: Decay of the coefficient of static friction with increasing velocity for PDMS on Si. Solid line added as a visual guide.

4.4 Comparison of Tested Systems

The measured quantity in each of our system is the maximum value of the dynamic friction coefficient. The maximum value was found by finding the point at which the direction of motion of the pipette tip changes relative to the motion of the substrate. These values were recorded for each applied normal force and velocity.

We found the variation of the friction coefficient with increasing velocity was able to be fit to the functional form of μ_k presented by Ruina [19], and Heslot *et al.* [20]. Although both of these models give similar expressions for the dynamic friction coefficient, the model by Heslot *et al.* offers more completeness in that it explains the variation of the static friction with contact time.

It is important to note that both of these models are based upon experimental evidence, and not a strict theoretical development. The logarithmic dependence of the coefficient of friction with changing velocity has been shown in many systems. The following discussion of the two models is meant to give a general overview of the assumptions within them, and the basis upon their formulation and not a strict derivation.

Ruina's model represent a generalized expression for a broad class of material contacts. This model is often termed the state-rate friction (SRF) model. State refers to the physical state of the material contact, and rate refers to the velocity of the substrate. The model is expressed by defining a friction function that is dependent on the velocity and system states, and also defining the rate of change of the state.

The generalized expressions for these functions are,

$$F_{friction} = F(V, \Theta_1, \Theta_2, ..., \Theta_n) \tag{4.1}$$

$$\dot{\Theta}_i = g_i(V, \Theta_1, \Theta_2, ..., \Theta_n), \tag{4.2}$$

where F is the friction function, V is the velocity, Θ_i is the state, and $\dot{\Theta}_i$ the derivative of the state with respect to time. For a single state variable, Ruina proposed functions based on experimentally determined variations in the friction coefficients with velocity change as represented by,

$$F_{friction} = f_0 + A\ln(V/V_0) + \Theta \tag{4.3}$$

$$\dot{\Theta}_i = -\frac{V}{L}[1 + B\ln(V/V_0)], \tag{4.4}$$

where f_0, B and A are coefficients to be fit to data and L represents the memory length. This memory length is the relative distance moved between surfaces at which all the initial contacts are broken and reformed. In the steady state case, the friction function and the expression for μ become,

$$F_{friction} = f_{ss0} + (A - B)\ln(V/V_0) \tag{4.5}$$

$$\mu_{ss} = \mu_{ss0} + \frac{1}{F_N}(A - B)\ln(V/V_0), \tag{4.6}$$

where A, B, f_{ss0}, μ_{ss0} and V_0 are expressions to be fitted and F_N is the normal force.

The variation of the steady state friction force may increase or decrease depending on the relative value of A to B.

Heslot's phenomenological model is based on results of their experiments [20]. From their experiments they came to several conclusions:

1. Friction at low velocities was controlled primarily be creep.

2. The time dependence of μ_s indicates slow relaxation.

3. μ_s and μ_d satisfy the relation $\mu_d(V) = \mu_s(D_0/V)$ indicating the presence of a memory length D_0.

4. the dynamics of the coefficient crosses from creep controlled to inertial controlled at some velocity.

The memory length in the work of Heslot *et al.* is the same as that was defined for Ruina's model. Creep controlled processes refer to the formation and breaking of asperity junctions or microcontacts between the two materials when they are in contact. As the velocity increases, it reaches a threshold where the system moves in a quasifree fashion and in which the friction force is dependent on the system inertia. For their work, Heslot *et al.* also found the velocity dependence of μ to be,

$$\mu = \alpha - \beta \ln(V/V_0), \tag{4.7}$$

where α and β are constants to be fit to the data and V_0 is a reference velocity (arbitrarily set at 1 μm/s so the argument of the logarithm is dimensionless). The

functional forms of for μ_k determined by Ruina and Heslot *et al.* are equivalent. Regardless of the details, the logarithmic dependence of the friction coefficient with changing velocity is commonly used to describe a broad range of data. The best fit coefficients for the systems tested in this work are shown in Table 4.1. The plots of the data along with the fits to Equation 4.7 are shown in Figure 4.5.

Table 4.1: Best fit coefficients for Equation 4.7. Errors shown are based on 95% confidence intervals.

System	α	β
PS on Si	0.17±0.06	0.05±0.06
PS on PS	0.42±0.14	0.17±0.1
PDMS on Si	0.081±0.025	0.029±0.015

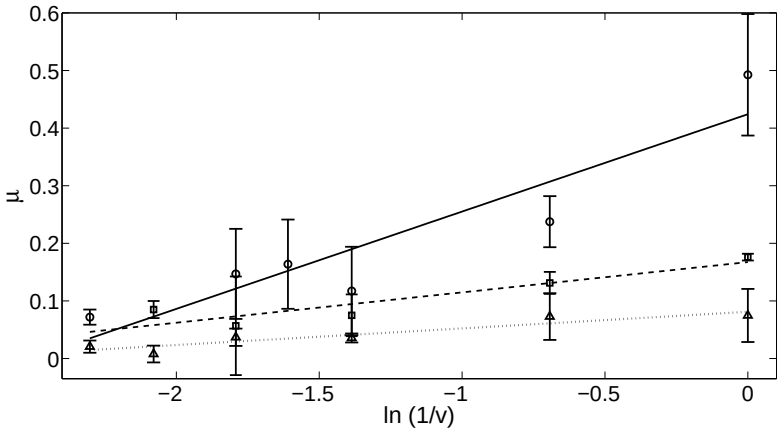

Figure 4.5: Plot of the coefficient of friction versus the $\ln(1/v)$, comparing all three systems. Fits are based on equation 4.7, with best fit coefficients given in Table 4.1.

The ratio of the coefficients for each system scales with the ratio of the measured friction coefficients. Also, the qualitative variation of the friction coefficients with increasing velocity agrees with previous research performed on metals [21], polymers

[22], and bristol board [20]. The results of our experiments also confirm the validity of the expressions for the coefficient of friction produced by Ruina and Heslot *et al.*.

4.5 Discussions

The results of our experiments show the ability of the measurement apparatus to reproduce reported coefficient values. They also showed the friction coefficient varied with increasing velocity according to known models. For example, the coefficient of friction for PS on PS at 1 μm/s agrees with known dry friction values. This result is most likely due to the fact that both the substrate and the bead are highly hydrophobic. As the two surfaces approach one another, it requires much less force to push the water out from between the two surfaces and allow the formation of a dry contact. The other example being PDMS on PS, which also agrees well with experiments that were performed by Bhushan *et al.* [18]. Although we do not have a direct comparison for lubricated PS on Si, our measured value is consistent with the presence of a lubricating layer of water between the PS bead and the Si substrate. In this system (as well as PDMS on Si), the bead is highly hydrophobic whereas the silicon oxide layer that likely resides on the surface of the Si wafer is hydrophilic. A greater amount of force (relative to PS on PS) would be required to push the water out from between the two surfaces and form a dry contact. Without adequate force, a thin film of water seperates the two materials and acts as a lubricant.

One of the major issues regarding our experimental apparatus concerns the symmetry of the recorded deflections as the substrate oscillates about an equilibrium position. The asymmetry in the lateral deflections may be indicative of a normal force that is not directed along the lateral pipette arm. In some cases, where the lateral arm is directed nearly perfectly normal to the surface, it may then correspond to a slope in the surface of the substrate. It may also be due to the spring constant of the lateral arm differing with the direction of deflection. Therefore making sure to align the substrate and the pipette properly is important in obtaining accurate force measurements. Generally, this asymmetry was handled through the manual manipulation of the the pipettes angle of attack. We also produced several pipettes for each experimental run and then tested them to see if we could produce symmetric deflections about the equilibrium point. Producing symmetric deflections about the initial position proved itself to be very difficult. We attempted to overcome the issue of asymmetric lateral deflections by producing a more symmetric pipette geometry (Figure 4.6). However, the new geometry was unsuccessful in producing consistently

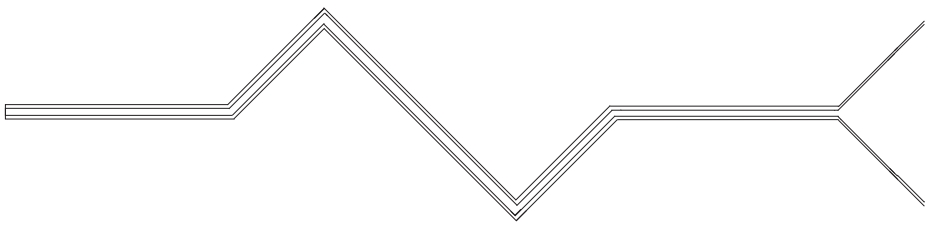

Figure 4.6: Symmetric pipette geometry.

symmetric deflections. The asymmetry was most likely due to the varying thickness

of the elongated portion of the pipette from its base to the tip. Other possible solutions may include the development of a model that takes the inherent asymmetry of the L-shaped pipette into account. Another potential solution would be to change the orientation of the pipette to the substrate surface. For example, if we were to rotate the pipette by 90 °, and move the substrate lateral to this new position as in Figure 4.7.

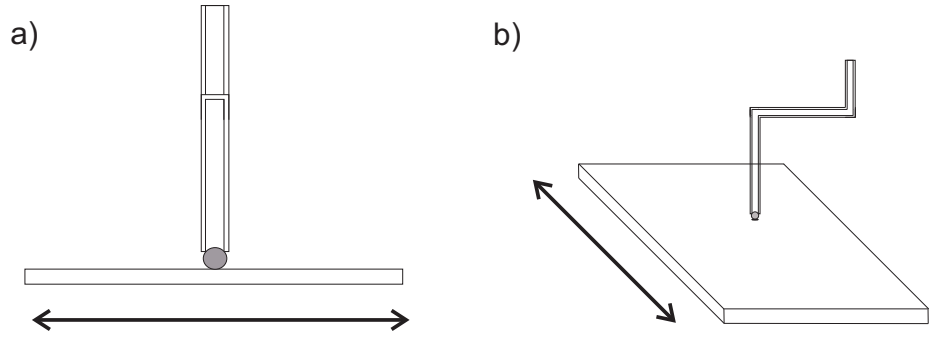

Figure 4.7: Substrate motion to produce symmetric force distribution about the axis of the pipette. ⓐ Sideview, ⓑ overhead perspective.

Our experimental apparatus was further validated by testing variation of the coefficient of friction with increasing velocity. The collected data for each of the experimental systems fits well to the heuristic model of Heslot *et al.*[20]. Although we cannot make the same conclusions as Heslot regarding his dry friction experiments, the model has been applied extensively to other systems (as was mentioned previously in the Results section).

Chapter 5

Conclusions

In this study, we have analyzed the ability of a micropipette to act as both a lateral and normal force transducer in friction experiments. Within each of these experiments, a PS bead (or PDMS coated PS bead) is grasped by the micropipette using suction applied by a syringe. The bead is then brought into contact with the substrate surface, and the substrate is then moved lateral to the pipette in an oscillating fashion about this initial position causing the lateral force producing arm to deflect. After this has been completed for several loops, the normal deflection is increased and the oscillations repeated. The deflections provide us with the forces produced by the pipette, where the force is proportional to the deflection. The constant relating the force and deflection is simply the spring constant of the pipette in the normal and lateral directions.

The analysis of our experiments was performed by image correlation. Initially, two dimensional correlation was used but due to the limited accuracy of the correlation in the direction normal to the substrate, we used one dimensional correlation for

the lateral deflection and motor position measurements for the change in normal deflection. The one dimensional correlation had been shown in previous work to be capable of achieving a $\approx 10 nm precision$[2].

The results of our experiments showed that the friction coefficient decreased logarithmically with increasing velocity. This result agrees with the heuristic models of Heslot *et al.* [20] and Ruina [19]. The values that were collected through our experimental work also agree with previously published results, where comparisons were possible. The major limitation of this experimental method is the large error present in our measurements. This would likely be reduced by fixing problems with the symmetry of the system, as a small amount of asymmetry was unavoidable in our measurements.

Based on the results of this study, the use of micropipettes as force transducers in friction experiments has been shown to be a both reproducible and consistent with known results. In the future, the simplicity and versatility of this technique will allow us to use it to more fully understand the dynamics of the membranes of living cells in contact with different surfaces and in various environments.

Bibliography

[1] M-A Goulet. Friction measurements on living hela cells, 2008.

[2] M-J Colbert. *Mechanics of Lipid Vesicles and Living Cells*. PhD thesis, McMaster University, 2010.

[3] H-J. Butt and M. Kappl. *Surface and Interfacial Forces*. Wiley-VCH Verlag GmbH Co. KGaA Weinheim, 2010.

[4] JC Burton, P. Taborek, and JE Rutledge. Temperature dependence of friction under cryogenic conditions in vacuum. *Tribology Letters*, 23(2):131–137, 2006.

[5] L. Shi, V.I. Sikavitsas, and A. Striolo. Experimental friction coefficients for bovine cartilage measured with a pin-on-disk tribometer: Testing configuration and lubricant effects. *Annals of biomedical engineering*, pages 1–15, 2011.

[6] M.R. Widmer, M. Heuberger, J. Voros, and N.D. Spencer. Influence of polymer surface chemistry on frictional properties under protein-lubrication conditions: implications for hip-implant design. *Tribology Letters*, 10(1):111–116, 2001.

[7] E. Kumacheva. Interfacial friction measurement in surface force apparatus. *Progress in surface science*, 58(2):75–120, 1998.

[8] S. Yamada and J. Israelachvili. Friction and adhesion hysteresis of fluorocarbon surfactant monolayer-coated surfaces measured with the surface forces apparatus. *The Journal of Physical Chemistry B*, 102(1):234–244, 1998.

[9] A. Artsyukhovich, L.D. Broekman, and M. Salmeron. Friction of the liquid crystal 8cb as probed by the surface forces apparatus. *Langmuir*, 15(6):2217–2223, 1999.

[10] M. Benz, N. Chen, and J. Israelachvili. Lubrication and wear properties of grafted polyelectrolytes, hyaluronan and hylan, measured in the surface forces apparatus. *Journal of Biomedical Materials Research Part A*, 71(1):6–15, 2004.

[11] C.M. Mate, G.M. McClelland, R. Erlandsson, and S. Chiang. Atomic-scale friction of a tungsten tip on a graphite surface. *Physical review letters*, 59(17):1942–1945, 1987.

[12] R. Bennewitz. Friction force microscopy. *Materials Today*, 8(5):42–48, 2005.

[13] JP Lewis. Fast template matching. In *Vision Interface*, volume 10, pages 120–123. Citeseer, 1995.

[14] K. Briechle and U.D. Hanebeck. Template matching using fast normalized cross correlation. In *Proceedings of SPIE*, volume 4387, pages 95–102. Spie, 2001.

[15] S. Bistac, A. Ghorbal, and M. Schmitt. Friction of polystyrene: Consequence on nano-wear. *Progress in organic coatings*, 55(4):345–354, 2006.

[16] N. Maeda, N. Chen, M. Tirrell, and J. Isrelachvilli. Adhesion and friction mechanisms of polymer-on-polymer surfaces. *Science*, 297(5580):379–382, 2002.

[17] Engineer's Handbook. Reference tables – coefficients of friction, June 2011.

[18] B. Bhushan and Z. Burton. Adhesion and friction properties of polymers in microfluidic devices. *Nanotechnology*, 16:467, 2005.

[19] A. Ruina. Slip instability and state variable friction laws. *J. geophys. Res*, 88(10):359–10, 1983.

[20] F. Heslot, T. Baumberger, B. Perrin, B. Caroli, and C. Caroli. Creep, stick-slip, and dry-friction: Experiments and a heuristic model. *Physical Review E*, 49(6):4973, 1994.

[21] P.E. Dupont and E.P. Dunlap. Friction modeling and control in boundary lubrication. In *American Control Conference, 1993*, pages 1910–1915. IEEE, 1993.

[22] T. Baumberger, P. Berthoud, and C. Caroli. Physical analysis of the state-and rate-dependent friction law. ii. dynamic friction. *Physical Review B*, 60(6):3928, 1999.